

Deformation microstructures of olivine in peridotite from Spitsbergen, Svalbard and implications for seismic anisotropy

H. JUNG,¹ W. MO¹ AND S. H. CHOI^{2*}

¹School of Earth and Environmental Sciences, Seoul National University, Seoul 151-747, Korea (hjung@snu.ac.kr)

²Korea Polar Research Institute, Songdo Techno Park, Incheon 406-840, Korea

ABSTRACT To understand the deformation mechanism and seismic anisotropy in the uppermost mantle beneath Spitsbergen, Svalbard, in the Arctic, the deformation microstructures of olivine in the peridotite of Spitsbergen were studied. Seismic anisotropy in the upper mantle can be explained mainly by the lattice-preferred orientation (LPO) of olivine. The LPOs of the olivine in the peridotites were determined using electron backscattered diffraction patterns. Eight specimens out of 10 showed that the [100] axis of the olivine was aligned subparallel to the lineation and that the (010) plane was subparallel to the foliation, showing a type A LPO. In the other two specimens the [100] axis of olivine was aligned subparallel to the lineation and both the [010] and [001] axes were distributed in a girdle nearly perpendicular to the lineation, showing a type D LPO. The dislocation density of the olivine in the samples showing a type D LPO was higher than that in the samples showing a type A LPO. The result of an Fourier transformation infrared study showed that both the types A and D samples were dry. These observations were in good agreement with a previous experimental study (*Tectonophysics*, **421**, 2006, 1): samples showing a type D LPO for olivine were observed at a high stress condition and samples showing both types A and D LPO were deformed under dry condition. Observations of both strong LPOs and dislocations of olivine indicate that the peridotites studied were deformed by dislocation creep. The seismic anisotropy calculated from the LPOs of the olivine could be used to explain the seismic anisotropy of *P*- and *S*-waves in the lithospheric mantle beneath Spitsbergen, Svalbard.

Key words: deformation microstructure; lattice-preferred orientation; olivine; peridotite; Spitsbergen.

INTRODUCTION

The study of the deformation microstructures of mantle rocks is important to understand the deformation mechanism and seismic anisotropy of the upper mantle (Nicolas & Christensen, 1987; Mainprice *et al.*, 2000; Karato *et al.*, 2008). Seismic anisotropy in the upper mantle around the world has been reported by many researchers (Fischer & Wiens, 1996; Smith *et al.*, 2001; Park & Levin, 2002; Nakajima & Hasegawa, 2004; Long & van der Hilst, 2005; Fouch & Rondenay, 2006) and used to constrain deformation and mantle flow within the Earth (Silver, 1996; Savage, 1999; Smith *et al.*, 2001; Park & Levin, 2002; Long & Silver, 2008). Seismic anisotropy in the upper mantle can be mainly explained by the lattice-preferred orientation (LPO) of olivine, which is a dominant mineral in the upper mantle (Hess, 1964; Nicolas & Christensen, 1987; Mainprice & Silver, 1993; Zhang & Karato, 1995; Mainprice *et al.*, 2000; Jung & Karato, 2001a; Kaminski & Ribe, 2001; Blackman *et al.*, 2002; Wenk, 2002; Jung *et al.*, 2006, 2009; Karato *et al.*, 2008).

Previous experimental studies of the deformation of olivine at high pressure and high temperature have

shown that the deformation microstructures, such as the LPO of olivine, are largely affected by many physical and chemical parameters, such as stress and water content (Jung & Karato, 2001a; Katayama *et al.*, 2004; Green & Jung, 2005; Jung *et al.*, 2006), temperature (Katayama & Karato, 2006), pressure (Jung *et al.*, 2009) and by chemical interactions among phases (Sundberg & Cooper, 2008). Several types of LPOs of olivine have been identified, including types A, B, C, D and E (Jung & Karato, 2001a; Katayama *et al.*, 2004; Jung *et al.*, 2006). Fabric studies of natural rocks have shown that each type of olivine LPO can be found in various places in the Earth. Type A LPO of olivine was commonly observed in rocks from the oceanic upper mantle (i.e. ophiolites) (Nicolas *et al.*, 1971; Mercier & Nicolas, 1975; Nicolas & Poirier, 1976; Mercier, 1985; Nicolas & Christensen, 1987; Ben Ismail & Mainprice, 1998; Mainprice *et al.*, 2000; Falus *et al.*, 2008; Skemer & Karato, 2008). Type D LPO of olivine was observed in the peridotites from the Bay of Island Ophiolite complex, Newfoundland (Mercier, 1985) and from the Baja California (San Quintin) (Mercier & Nicolas, 1975). Types B, C and E LPOs of olivine have been reported in rocks from convergent boundaries (Möckel, 1969; Tommasi *et al.*, 2000; Frese *et al.*, 2003; Mehl *et al.*, 2003; Mizukami *et al.*, 2004; Katayama *et al.*, 2005; Skemer *et al.*, 2006; Xu *et al.*,

*Present address: Department of Earth and Environmental Sciences, Chungnam National University, Daejeon 305-764, Korea.

2006; Michibayashi *et al.*, 2007; Warren *et al.*, 2008; Jung, 2009).

The seismic anisotropy under Spitsbergen dramatically changes with depth (Pilidou *et al.*, 2004, 2005). At a depth of 100 km below the study area, the fast directions of *S*-wave polarizations are nearly parallel to the presumed mantle flow (Nansen Ridge to the Yermak Plateau). At a depth of 150 km, the fast directions deviate significantly from the flow direction. At a depth of 200 km and below, the fast directions are nearly normal to the flow direction. It is still not fully understood what causes the seismic anisotropy.

The purpose of this study was to analyse the deformation microstructures of olivine, such as the LPO, along with the dislocation microstructures of olivine in the peridotite of Spitsbergen, Svalbard, and then compare the deformation microstructures of the natural samples with previous experimental studies, to understand the deformation mechanism and seismic anisotropy observed in the upper mantle beneath the study area.

GEOLOGICAL SETTING

Samples were collected from Sverrefjell in North-western Spitsbergen in Svalbard. Sverrefjell is one of the Quaternary volcanic centres and it contains abundant mantle xenoliths. The Svalbard is an archipelago in the Arctic Ocean, located midway between Norway and the North Pole (Fig. 1a). Spitsbergen is the largest island ($\sim 40,000 \text{ km}^2$) of the Svalbard archipelago. The basement rocks are the Proterozoic to Palaeozoic Hecla Hoek succession, which was metamorphosed and strongly deformed during the Caledonian orogeny (*c.* 450–400 Ma) (Amundsen *et al.*, 1987). In the study area, the Hecla Hoek succession consists of felsic gneisses, amphibolites and metasedimentary rocks. On northern Spitsbergen, a large complex graben, bounded by N–S faults, is filled with several kilometres of Devonian clastic redbeds (Fig. 1b).

Quaternary volcanic activity is found in the Bockfjord area (Fig. 1b) which exhibits significant evidence of Cenozoic uplift associated with mantle lithosphere thinning (Våagnes & Amundsen, 1993). An example of this activity is Sverrefjell, an eroded composite basaltic volcano 500 m high and 2 km in diameter. It contains abundant xenoliths of uppermost mantle and deep crustal rocks. Volcanological and geomorphological observations suggest that Sverrefjell grew prior to, and during, the last major glaciations of the area (*c.* 100,000 years ago) (Amundsen *et al.*, 1987). This young age is consistent with the presence of active hot springs north and south of Sverrefjell along the fault line and with K–Ar ages of the basalts ($< 1 \text{ Ma}$) (Burov & Zagruzina, 1976).

Tectonically, Svalbard is located on the north-westernmost edge of the Eurasian plate and near the Knipovich Ridge and Nansen Ridge, which are in the northern part of the Atlantic Ridge (Fig. 1a). The two

ridges have been linked by so-called ‘Spitsbergen Transform Zone’, representing short ridge segments connected by transform faults, and a fold zone caused by the Svalbard and Greenland collision at *c.* 65–60 Ma. Two distinct phases of volcanism in Neogene and Quaternary are known in Spitsbergen. The volcanic centres are bound to N–S trending faults which project towards the Yermak Plateau and parallel the Spitsbergen Transform Zone (Fig. 1) (Crane *et al.*, 1982; Tuchschnid & Spillmann, 1992). The faults are deep fractures at least Devonian in age, and were reactivated during continental fragmentation (Amundsen *et al.*, 1987). Quaternary volcanism in Spitsbergen is thus considered to be related to the activity of the spreading centre and transform fault zone $\sim 150 \text{ km}$ away.

METHODS

Sample collection

Samples were collected at Sverrefjell, Spitsbergen, during a field excursion in the summer of 2007. The study area was composed of reworked volcanic materials and mantle xenoliths. Large xenolith samples with diameters of $> 10 \text{ cm}$ were collected over the area of $\sim 50 \times 3 \text{ m}$ from marine terraces that developed on the flank of the volcano. Figure 2a shows an example of the mantle xenoliths found in the study area. Details of the occurrence of these mantle xenoliths were described in Skjelkvale *et al.* (1989).

Determination of foliation and lineation of specimen

Ten samples showing well-developed foliation were studied. The foliation was determined by the layering defined by aligned clinopyroxene or spinel. Samples were cut parallel to the foliation plane (*X–Y* plane) and a thin section was taken from the plane. The lineation was then determined using the method of Panozzo (1984) (Fig. 2b), which showed the most dominant direction of the grain boundaries in the *X–Y* plane. A thin section was cut parallel to the lineation (*X*) and perpendicular to the foliation (*Z*) to observe the microstructures of the specimen.

Analysis of mineral chemistry

The mineral compositions of Spitsbergen peridotites were analysed using a JXA-8900R wave-length-dispersive electron microprobe using ZAF matrix correction at Seoul National University. The machine was operated with an accelerating voltage of 15 kV, a beam current of 10 nA, beam diameter of $1 \mu\text{m}$ and 20 s counting time. Natural minerals were used as standards. Analytical results reported in Table S1 generally represent averages of five or more analyses of each grain and several grains from different parts of each sample. The minerals in all of the Spitsbergen peridotites do not show chemical zoning and are nearly homogeneous with no grain-

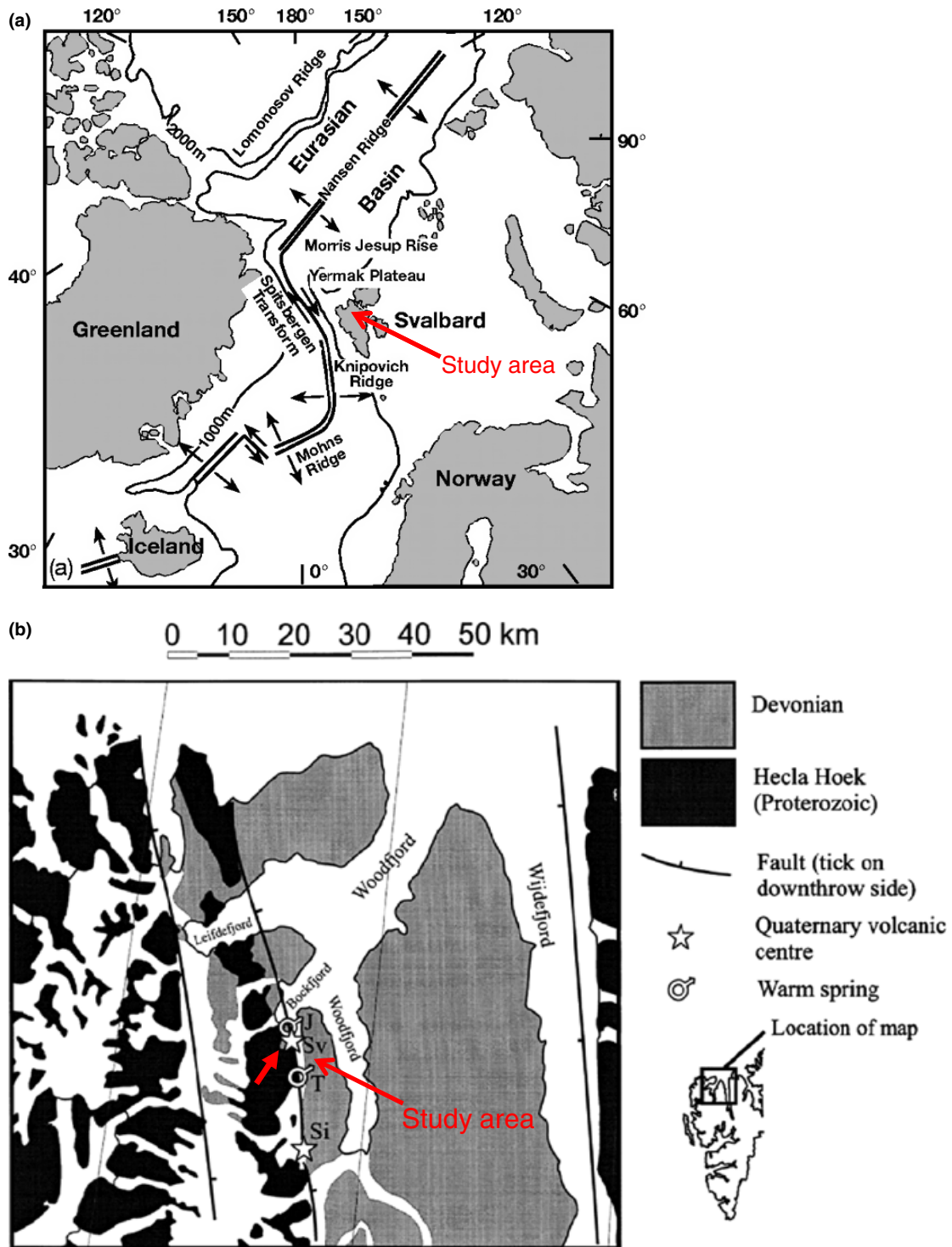


Fig. 1. A sketch map of the North Atlantic and Svalbard Archipelago (a) and the study area of northern Spitsbergen, (b) showing major geological and tectonic features. Sv, Sverrefjell; Si, Sigurdfjell; J & T, Jotun & Troll springs. White areas in (b) represent glacial region. (a) After (Amundsen *et al.*, 1987; Ionov *et al.*, 2002). (b) After (Banks *et al.*, 1998).

to-grain chemical variation, except at pyroxene and spinel contacts with the host basalt which display a reaction with the basalt within 400 μm from the contact boundary. All of the reported values are far from the

reaction boundary. As there was no meaningful chemical variation in the rock specimen studied, it suggests that the layering by aligned clinopyroxene or spinel formed by dynamic processes.

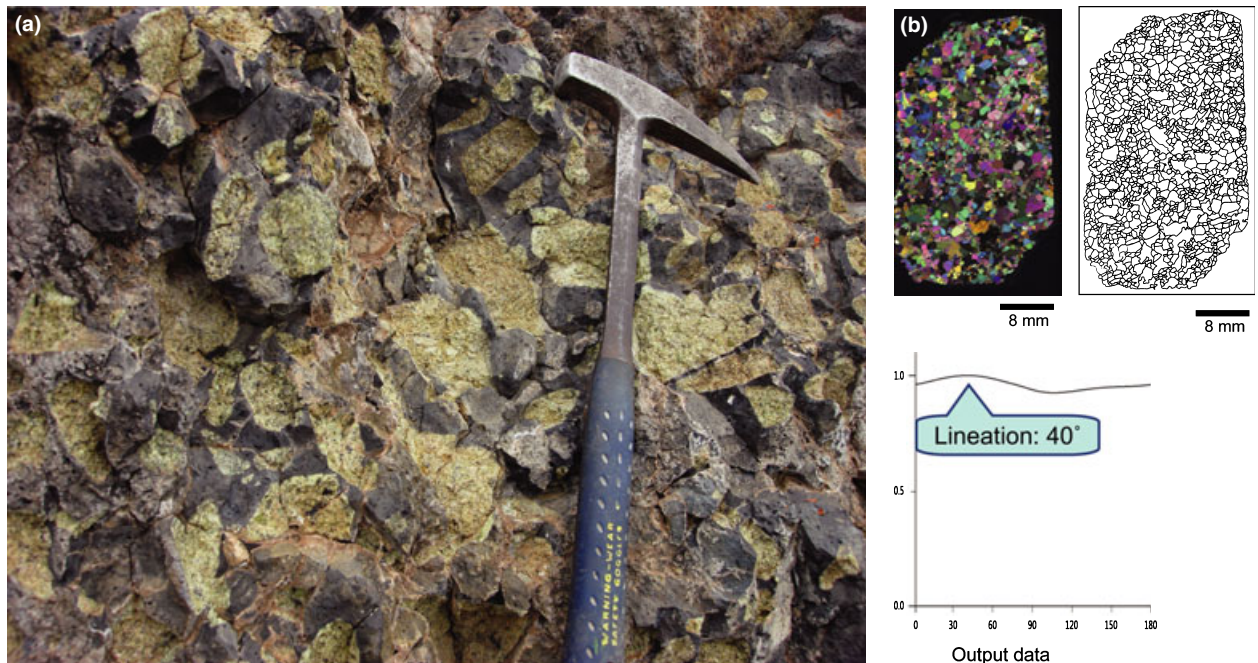


Fig. 2. (a) An example of mantle xenoliths in the study area. (b) Optical photomicrograph and a drawing of grain boundaries of the specimen SVF-66. Lineation was determined on the foliation (X - Y plane) using the method (Panozzo, 1984).

Determination of LPO

To determine the LPO of the olivine, electron back-scattered diffraction (EBSD) patterns (Dingley, 1984; Lloyd, 1987; Prior *et al.*, 1999) were used. The HKL EBSD system attached to the JEOL JSM-6380 SEM at SEES in the Seoul National University was used in this study. Samples were polished using a 1 μm diamond paste and then, to remove all of the surface damage, the specimens were polished using SYTON (0.06 μm colloidal silica) fluid for chemical-mechanical polishing (Lloyd, 1987). The specimens were coated with ~ 3 nm thick carbon layer to prevent charging in the SEM. The specimen surface was inclined at 70° to the incident beam. EBSD patterns were collected on a phosphor screen, where the experimental conditions were an accelerating voltage of 20 kV, a working distance of 15 mm and a spot size of 60. All of the EBSD patterns were manually indexed using the HKL's Channel 5 software at the Tectonophysics Laboratory at SEES in SNU.

Observation of dislocation microstructures

To observe the dislocation microstructures of the olivine, samples were coated with oxygen (Kohlstedt *et al.*, 1976) and observed in the JEOL JSM-6380 SEM using the backscattered electron mode (Karato, 1987; Jung & Karato, 2001b). The oxygen coating of the samples took place in an oven at 800°C for 1 h. Samples were coated with oxygen as a result of the precipitation of either magnetite or hematite on the

dislocation lines. Each sample surface was then gently polished to remove a thin layer of oxides. The SEM was operated at 15 kV acceleration voltage, 10 mm working distance and a spot size of 60.

Determination of water content of specimen

Fourier transformation infrared (FTIR) spectroscopy was used to determine the hydroxyl concentration in a sample. All of the samples were polished on both sides to a 110–260 μm thickness and were kept in an oven at 120°C for more than 1 day before an FTIR measurement was made. A Nicolet 6700 instrument with a Continuum IR Microscope was used at the Tectonophysics Laboratory at SEES in Seoul National University. The water content within a single crystal was measured using an IR beam size of $50 \times 50 \mu\text{m}$. Nitrogen gas was flushed during the FTIR measurement to avoid measuring the moisture in the atmosphere. The measurements were carried out using an unpolarized light source, a KBr beam-splitter and an MCT detector. A series of 128 scans was averaged for each spectrum with a resolution of 4 cm^{-1} .

RESULTS

Ten spinel peridotite xenoliths were studied from Spitsbergen, Svalbard and the results are summarized in Table 1. The xenoliths show microstructures of equigranular texture (Fig. 3a,c) to porphyroclastic texture (Fig. 3e,g) according to Mercier & Nicolas,

(1975). Kink bands are commonly observed in olivine in all specimens.

Mineral chemistry

The mineral compositions of Spitsbergen peridotites studied are typical of mantle phases: forsterite-rich olivine, enstatite-rich orthopyroxene, diposide-rich clinopyroxene and Cr-rich spinel (Table S1). Olivine shows a very narrow range of Mg-numbers [$Mg\# = 100Mg/(Mg + \Sigma Fe)$] of 89.9–91.9, and have 0.03–0.20 wt% CaO, 0.34–0.70 wt% NiO and 0.09–0.15 wt% MnO concentrations (Table S1). Orthopyroxene is enstatite with a composition of $Wo_{0.9-1.4}En_{89.4-91.1}Fs_{7.8-9.5}$. The Al_2O_3 and Cr_2O_3 concentrations are in the range 1.9–4.1 wt% and 0.2–0.5 wt% respectively. Orthopyroxene has Mg# between 91.3 and 97.1 that shows a good positive correlation with, but slightly higher than, that of coexisting olivine. Clinopyroxene is diopside with a composition of $Wo_{45.5-47.5}En_{48.2-50.0}Fs_{3.6-4.7}$. It has Mg# between 91.7 and 98.6 that shows a positive correlation with that of coexisting orthopyroxene. The Na_2O , TiO_2 , Al_2O_3 and Cr_2O_3 concentrations have a range of 1.0–1.7, 0.1–0.6, 3.5–6.4 and 0.6–1.1 wt% respectively. Al_2O_3 contents are positively correlated with Na_2O and TiO_2 , but negatively with Cr_2O_3 contents respectively. Spinel is a chromian spinel with highly variable Cr-numbers [$Cr\# = 100Cr/(Cr + Al)$] of 8.5–50.3 and Mg# of 61.7–80.1. The Mg# of the spinel shows a good negative correlation with their Cr#. Furthermore, Cr# of spinel is positively correlated with Mg# of coexisting olivine and pyroxene (Table S1), indicating that they are equilibrated in the spinel peridotite field.

Estimation of temperature and pressure

Equilibration temperatures are estimated from the electron microprobe data using two-pyroxene thermometers of Wells (1977) and Bertrand & Mercier (1985) modified by Brey & Köhler (1990). The equilibration temperatures range from 850 to 1000 °C

(Table S1), which are within the range 840–1170 °C reported for Spitsbergen peridotites by Amundsen *et al.* (1987) and Ionov *et al.* (2002). The two-pyroxene thermometers yield consistent results (within 30 °C) for the xenoliths. Projection of the temperature estimates onto the geotherm for north-western Spitsbergen after Amundsen *et al.* (1987) yields pressures of 7–11 kbar.

LPO of olivine

The LPOs of olivine were measured using the HKL EBSD system and the results are summarized in Table 1. The LPOs of the olivine in all of the samples were strong. These are shown in a pole figure (Fig. 4). Eight specimens out of 10 showed that the [100] axis of the olivine was aligned subparallel to the lineation and that the [010] axis was aligned subparallel to normal for the foliation, showing the type A LPO (Jung *et al.*, 2006). Two specimens showed that the [100] axis of the olivine was aligned subparallel to the lineation and that both the [010] and [001] axes were distributed in a girdle nearly perpendicular to the lineation, indicating a type D LPO (Jung *et al.*, 2006). The LPO results for the olivine indicated that the specimens were deformed at low stress below ~300 MPa (for the samples showing the type A LPO) or at high stress above ~300 MPa (for the samples showing the type D LPO) under a dry condition, based on previous experimental data (Jung & Karato, 2001a; Jung *et al.*, 2006). The strength of the LPO of the olivine was calculated (Table 1) and is shown as a misorientation index (M-index) (Skemer *et al.*, 2005). Sample SVF-66 showed the highest strength for the LPO of the olivine, with an M-index of 0.27.

Water content

Unpolarized FTIR spectra from samples are presented in Fig. 5. A range of wave numbers 3000–3800 is shown because the region was dominated by the stretching vibrations of O–H bonds (Paterson, 1982). The infrared beam is absorbed in the wavenumber

Table 1. Sample description and results.

Sample	Grain aspect ratio ^a	Olivine LPO type	Slip system of olivine	M-index of olivine ^b	FTIR sample thickness (μm)	Water Content (ppm H/Si) ^c	Vp anisotropy (%)	Max dVs anisotropy (%)	Mean grain size (μm) ^d	Estimated stress (MPa) ^e
SVF-04	1.06	A	(010) [100]	0.15	150	70 ± 20	9.2	6.4	1000	10 ± 5
SVF-05	1.13	A	(010) [100]	0.15	140	60 ± 20	8.4	5.9	880	11 ± 5
SVF-27	1.14	A	(010) [100]	0.18	150	40 ± 20	11.1	6.9		
SVF-30	1.17	A	(010) [100]	0.15	120	70 ± 20	9.5	5.9		
SVF-49	1.14	D	(0k1) [100]	0.20	250	50 ± 20	11.9	7.6	310	21 ± 5
SVF-66	1.06	A	(010) [100]	0.27	160	120 ± 20	13.6	8.2		
SVF-67	1.11	A	(010) [100]	0.12	110	160 ± 20	8.5	5.5		
SVF-70	1.17	A	(010) [100]	0.14	260	40 ± 20	9.0	5.8		
SVF-71	1.18	A	(010) [100]	0.12	260	60 ± 20	8.6	5.4		
SVF-72	1.06	D	(0k1) [100]	0.08	110	130 ± 20	7.8	5.5	480	16 ± 5

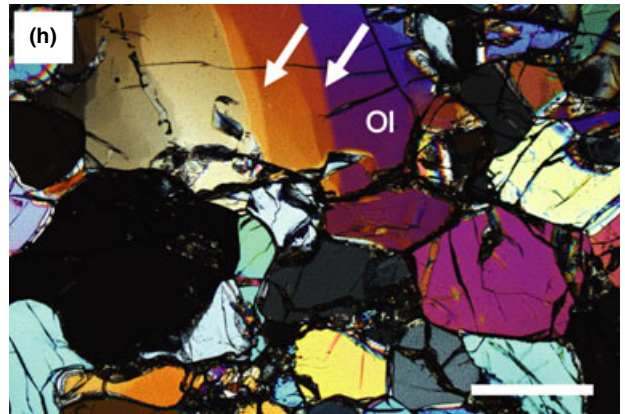
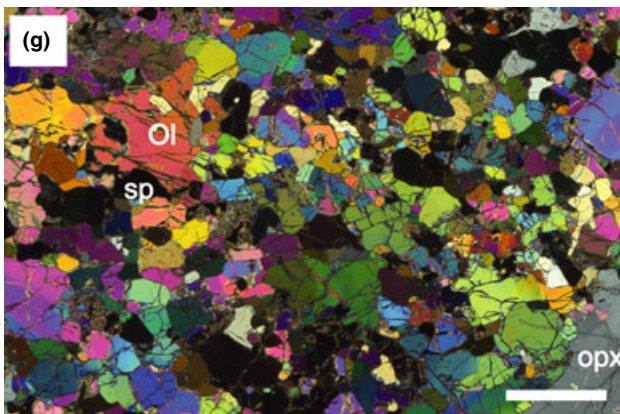
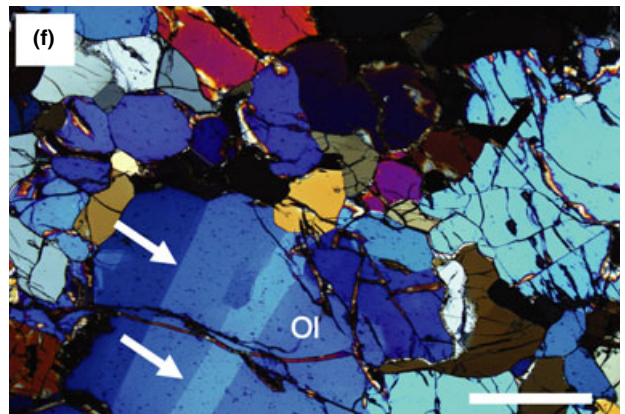
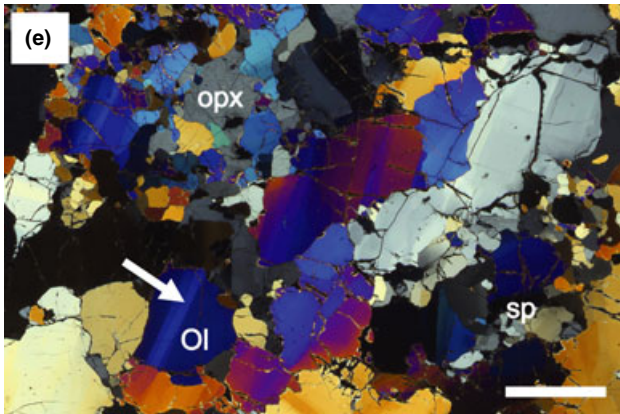
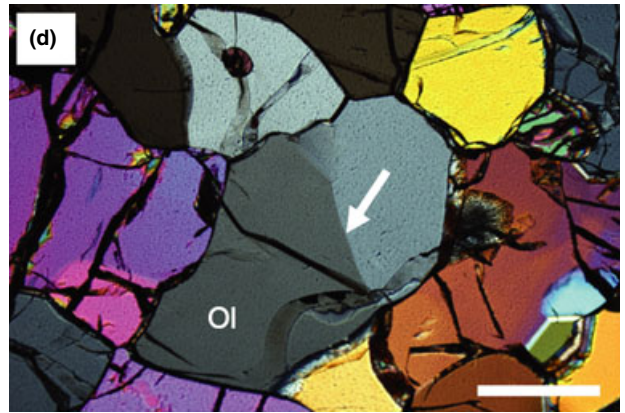
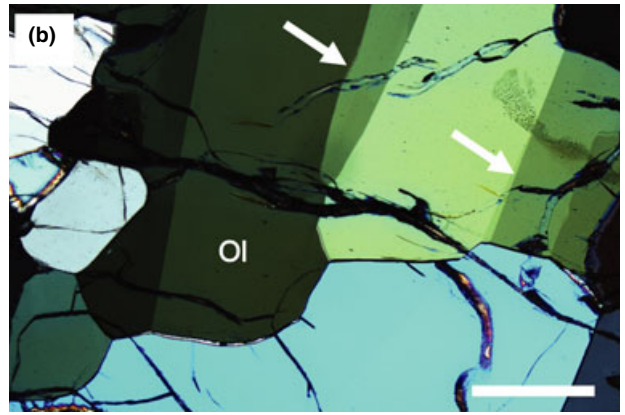
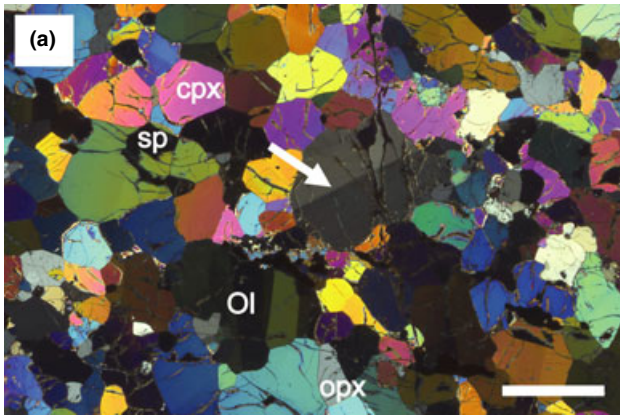
^aGrain aspect ratio was measured in foliation (X – Y plane).

^bM-index is the misorientation index which shows the fabric strength of olivine (Skemer *et al.*, 2005).

^cWater content of olivine was measured by FTIR using a calibration of Paterson (1982). If a calibration by Bell *et al.* (2003) is used, the result should be multiplied by a factor of ~3.5.

^dRecrystallized grain size was measured using the linear intercept method (Gifkins, 1970).

^eStress was estimated using the relationship between stress and recrystallized grain size under dry condition (Jung & Karato, 2001b).



range 3567–3750 cm^{-1} . A small IR peak was observed at 3567 or 3570 cm^{-1} in most of the samples. This peak shows the presence of a small amount of water in olivine (Kohlstedt *et al.*, 1996). A few samples showed IR peaks at wavenumber of 3629, 3649 and 3750 cm^{-1} . The results of the FTIR study are summarized in Table 1. The water content was estimated using a calibration by Paterson (1982). The FTIR data showed that all of the olivine samples contained a small amount of water (40–160 ppm H/Si) and were dry. If the Bell *et al.* (2003) calibration is used to calculate water content from FTIR spectra, the result should be multiplied by a factor of 3.5. For olivine LPO (e.g. Jung & Karato, 2001a; Jung *et al.*, 2006, 2009; Karato *et al.*, 2008), a water content of <200 ppm H/Si is considered dry according to the Paterson calibration (as is a water content of <700 ppm H/Si according to the Bell *et al.* calibration). No correlation was found between the type of olivine LPO (type A v. type D) or other characteristics (e.g. water content) and the location of the samples.

Observation of dislocation microstructures

The dislocation microstructures of the olivine after oxygen coating (Karato, 1987; Jung & Karato, 2001b) are shown in Fig. 6. In general, the dislocation distributions for all of the samples were heterogeneous. However, the overall dislocation density of the olivine in the sample showing the type D LPO (SVF-49) was higher than that in the sample showing the type A LPO (SVF-71). Numerous subgrain boundaries are observed in types A and D samples (dry specimen) (Fig. 6). This is also in good agreement with the result of a previous experimental study on the deformation of olivine at high pressure and high temperature (Jung & Karato, 2001b; Jung *et al.*, 2006).

Inverse pole figures

To infer a dominant slip system for the olivine, inverse pole figures were generated by plotting the direction of interest into the sample space. The inverse pole figures for the olivine in the direction of lineation and foliation normal are shown in Fig. 7. The inverse pole figures show that, for the samples showing the type A LPO, the [100] axes of the olivine were aligned subparallel to the lineation and the [010] axes were aligned subnormal to the foliation (Fig. 7), indicating that the

[100] axis was a dominant slip direction and the (010) plane was a dominant slip plane: the (010)[100] slip system. For the samples showing the type D LPO (SVF-49 & -72), the [100] axes of the olivine were concentrated subparallel to the lineation. However, a weak distribution of the [010] and [001] axes of the olivine were observed in the direction of the foliation normal, indicating that the [100] axis was a dominant slip direction, but the slip plane was not well defined: the (0kl)[100] slip system.

Estimation of stress

A grain-size piezometer was used for olivine under a dry condition (Jung & Karato, 2001b) to estimate the stress of the specimens showing both types A and D LPOs. The recrystallized grain size was measured by the linear intercept method, using the stereographic correction factor of 1.5 for 3D (Gifkins, 1970). The average grain size of the samples showing the type A LPO was 880–1000 μm (Table 1). On the other hand, the average grain size of the samples showing the type D LPO was 310–480 μm . The levels of stress required for the deformation of the recrystallized grains for the types A and D samples were determined to be 10 ± 5 MPa and 20 ± 5 MPa (Fig. 8) respectively. The linear relationship between differential stress and recrystallized grain size (Fig. 8, Jung & Karato, 2001b) was obtained using data from a study by Jung & Karato (2001b) and from other previous studies (Karato *et al.*, 1980; van der Wal *et al.*, 1993; Zhang *et al.*, 2000). The stress was estimated from the dislocation densities of 30–50 grains for each sample in the Jung & Karato (2001b) experiment. It should also be noted that van der Wal *et al.* (1993) and Zhang *et al.* (2000) precisely estimated the stress from the external load cell using the Paterson apparatus. The grain-size piezometer can be extrapolated to lower stresses and higher grain sizes than those measured by Jung & Karato (2001b) with an uncertainty of $\sim 20\%$. This uncertainty value takes into account the uncertainty in the estimation of stress from the scatter in the dislocation density of a single sample and uncertainties in temperature and pressure during the experiment.

Stress was also estimated from the dislocation densities of samples using the oxygen decoration technique. The dislocation densities for SVF-71 and SVF-49 were measured from the total length of dis-

Fig. 3. Optical photomicrographs of microstructures within the analysed peridotite samples. All images were taken under crossed polarized light. Kink bands (white arrows) are commonly observed in olivine. (a, b) Sample SVF-04. Coarse equigranular texture. Olivine grains show undulose extinction and have serrated grain boundaries. (c, d) Sample SVF-05. Equigranular texture. The microstructure is homogeneous and grains are elongated up to aspect ratios of 2:1. (e, f) Sample SVF-49. Porphyroclastic texture. Numerous kink bands are observed. Porphyroclasts are several millimetres in size and are locally elongated up to aspect ratios of 3:1. Dynamically recrystallized grains are observed next to porphyroclasts. (g, h) Sample SVF-72. Porphyroclastic texture. The microstructure is relatively heterogeneous. Some grains show kink bands and contain numerous inclusions. Scale bars represent 2 mm for the figures (a, c, e & g) and 500 μm for the figures (b, d, f & h). Ol, olivine; opx, orthopyroxene (enstatite); cpx, clinopyroxene (diopside); sp, spinel.

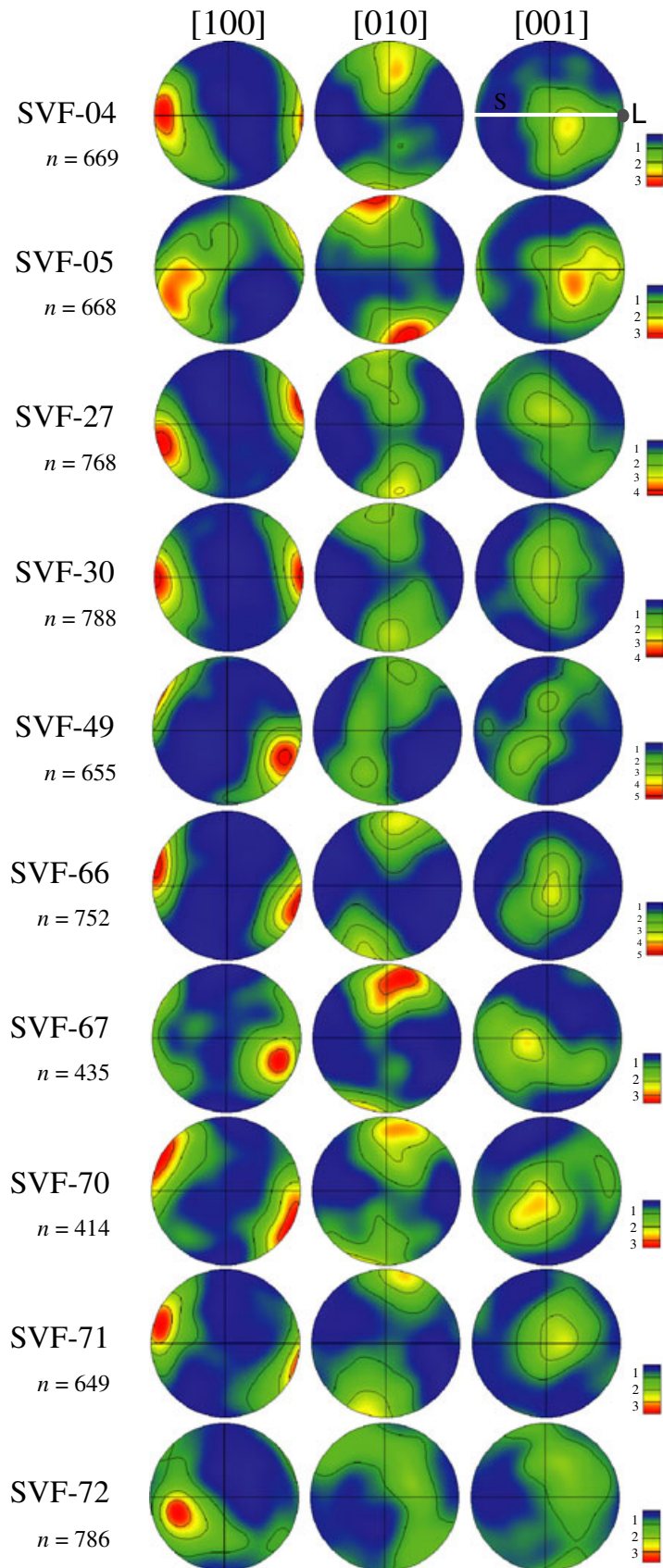


Fig. 4. Pole figures of crystallographic orientation of olivine are presented in the upper hemisphere using an equal area projection. The colour coding refers to the density of data points (the numbers in the legend correspond to the multiples of uniform distribution). A half scatter width of 30° was used. S, foliation; L, lineation; n, number of grains.

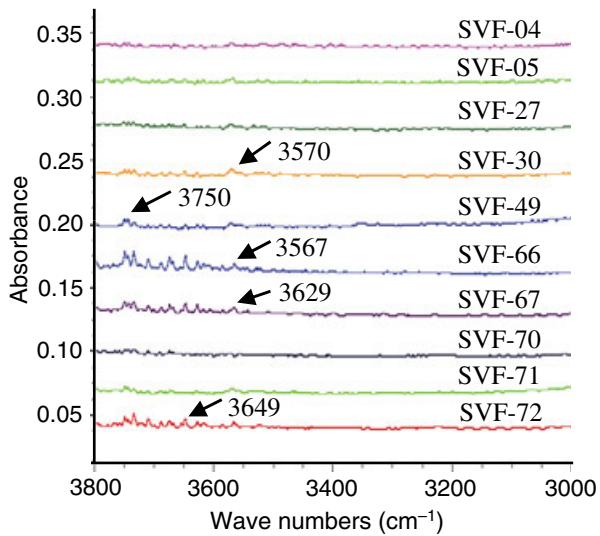


Fig. 5. Unpolarized FTIR spectra of olivine in each specimen. The infrared beam size of $50 \times 50 \mu\text{m}$ was used in the transmission mode. Water content in olivine was calculated using the calibration (Paterson, 1982) and given in Table 1.

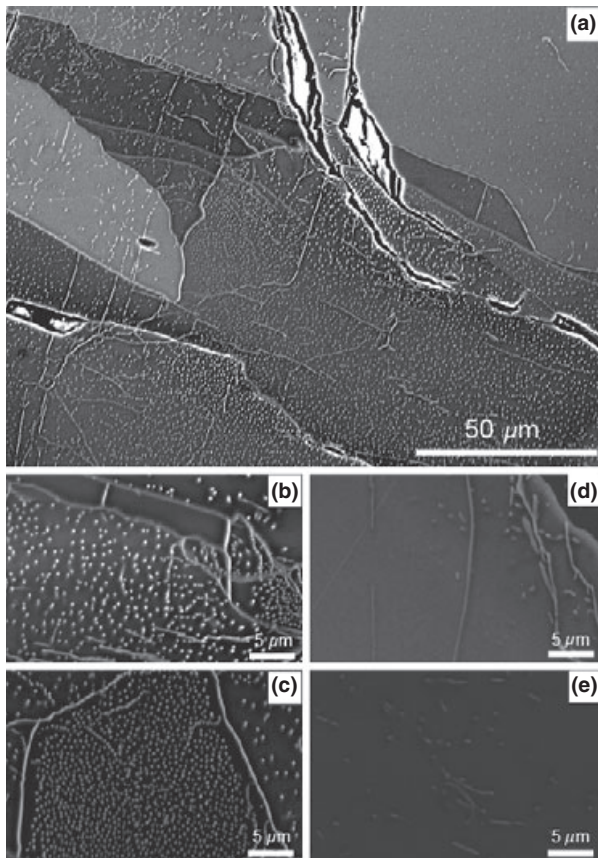


Fig. 6. Backscattered electron (BSE) images showing dislocation microstructures of olivine in the specimen SVF-49 (a–c) and specimen SVF-71 (d, e). White dots and lines are dislocations and sub-boundaries.

location lines measured by scanning electron microscopy (Karato, 1987; Jung & Karato, 2001b). Thirty grains (corresponding to a volume of $5300 \mu\text{m}^3$) were used for each sample. The dislocation densities for SVF-71 and SVF-49 were $1.9 \times 10^{11} \text{m}^{-2}$ and $3.8 \times 10^{11} \text{m}^{-2}$ respectively. The stress from the dislocation densities for SVF-71 and SVF-49 were measured using the calibration method of Jung & Karato (2001b) and Karato & Jung (2003). The stresses for SVF-71 and SVF-49 were determined to be $21 \pm 5 \text{MPa}$ and $34 \pm 7 \text{MPa}$ respectively. The stress needs to be considered as an upper limit because dislocation-free grains ($\sim 30\%$ of the grains in a specimen) were ignored in the estimations of the dislocation densities. In this study, the stresses estimated from the dislocation densities are comparable with those estimated using a grain-size piezometer (10 ± 5 to $20 \pm 5 \text{MPa}$).

Seismic anisotropy

Seismic velocity and seismic anisotropy were calculated using the orientation data (Mainprice, 1990) from the EBSD analysis of olivine, where the elastic constants of a single crystal olivine (Abramson *et al.*, 1997) were used. As olivine is elastically anisotropic and was the dominant mineral in the rock specimen, it controlled the overall seismic velocity and seismic anisotropy of the peridotite. Figure 9 shows the results for the seismic velocity (V_p and V_s) and seismic anisotropy of shear waves in a pole figure. An aggregate of 100% olivine was assumed for the calculation of the seismic anisotropy. Most samples contained olivine (50–85%), Opx (10–20%), Cpx (2–25%) and a very small quantity of spinel. The P -wave (V_p) exhibited strong seismic anisotropy in the range of 7.8–13.6%. The maximum anisotropy of the shear wave (dV_s) was in the range of 5.4–7.6%. This is considerably stronger than the value often inferred for upper mantle shear wave anisotropy. Our estimation of seismic anisotropy is considered an upper limit because other phases such as Opx, Cpx and spinel are known to reduce the strength of seismic anisotropy. All of the specimens showed that the polarization direction of the faster shear wave (V_{s1} polarization) was subparallel to the lineation (flow direction), independent of the fabric type (type A or D) (Fig. 9).

DISCUSSION

Deformation microstructures of olivine: natural rocks v. experimental samples

Two types of strong LPOs for olivine were observed in the peridotites from Spitsbergen, Svalbard (Fig. 4). The type A LPO of olivine was observed in the samples with a large grain size. In contrast, the type D LPO of olivine was observed in the samples with a small grain size. The recrystallized grain size was used to estimate the stress of the samples. Samples showing the type A LPO had a large grain size, giving a low stress value of

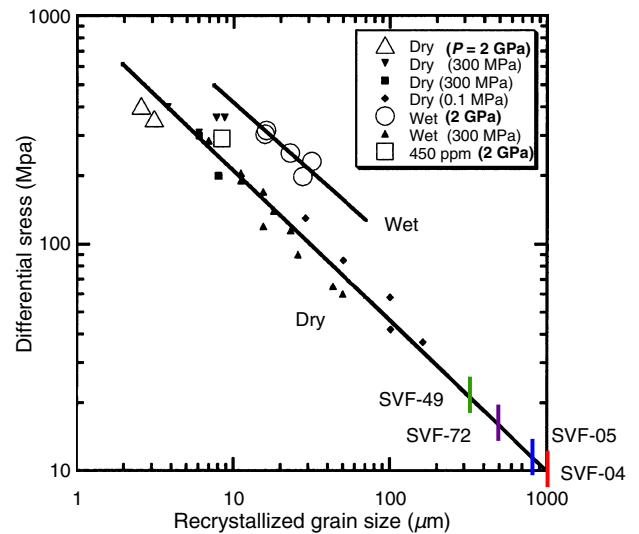
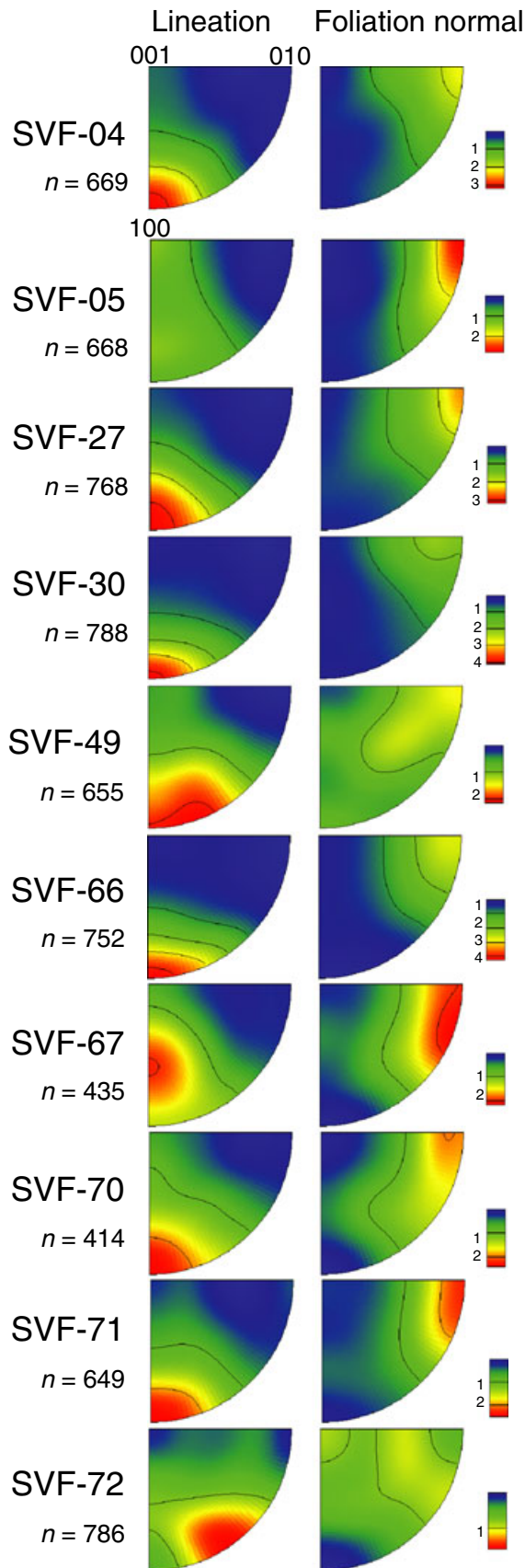


Fig. 8. Stress *v.* recrystallized grain-size relationship. The solid lines indicate the results of dry and wet experiments. The stresses of four samples were estimated using the solid line for dry experiments. The four bars represent the four samples. Red: SVF-04; blue: SVF-05; violet: SVF-72; green: SVF-49. Modified after (Jung & Karato, 2001b).

10 ± 5 MPa during the deformation of the specimen. Samples showing the type D LPO had a small recrystallized grain size, giving a high stress value of 20 ± 5 MPa. The observation of high stress for the specimens showing the type D LPO was consistent with the observations of the dislocation microstructures of the specimens. Samples showing the type D LPO showed higher dislocation densities ($3.8 \times 10^{11} \text{ m}^{-2}$, meaning high stress was experienced: $34 \pm 7 \text{ MPa}$, stress estimation of an upper bound) than those showing the type A LPO. This is in good agreement with the previous experimental samples of olivine deformed at high pressure and high temperature (Jung & Karato, 2001a; Jung *et al.*, 2006).

There is a difference between the stress conditions in Jung *et al.* (2006) and the differential stresses in this study (~5–25 MPa). The differential stresses in most experiments are much higher (~100–300 MPa) than those inferred here. Future studies should concentrate on developing a scaling law to compare experimental results to natural samples. Katayama & Karato (2006) showed that there is a temperature effect on the LPO of olivine. Furthermore, the differential stress for the types B and C LPO transition is predicted to occur at 1 MPa and 730 °C. This implies that the stress associated with natural LPO development could be low at low temperatures.

An FTIR study of all of the olivine samples showed that the olivine contained very small amounts

Fig. 7. Inverse pole figures of olivine. A half scatter width of 30° was used. The colour coding refers to the density of the data points. *N* is the number of grains analysed.

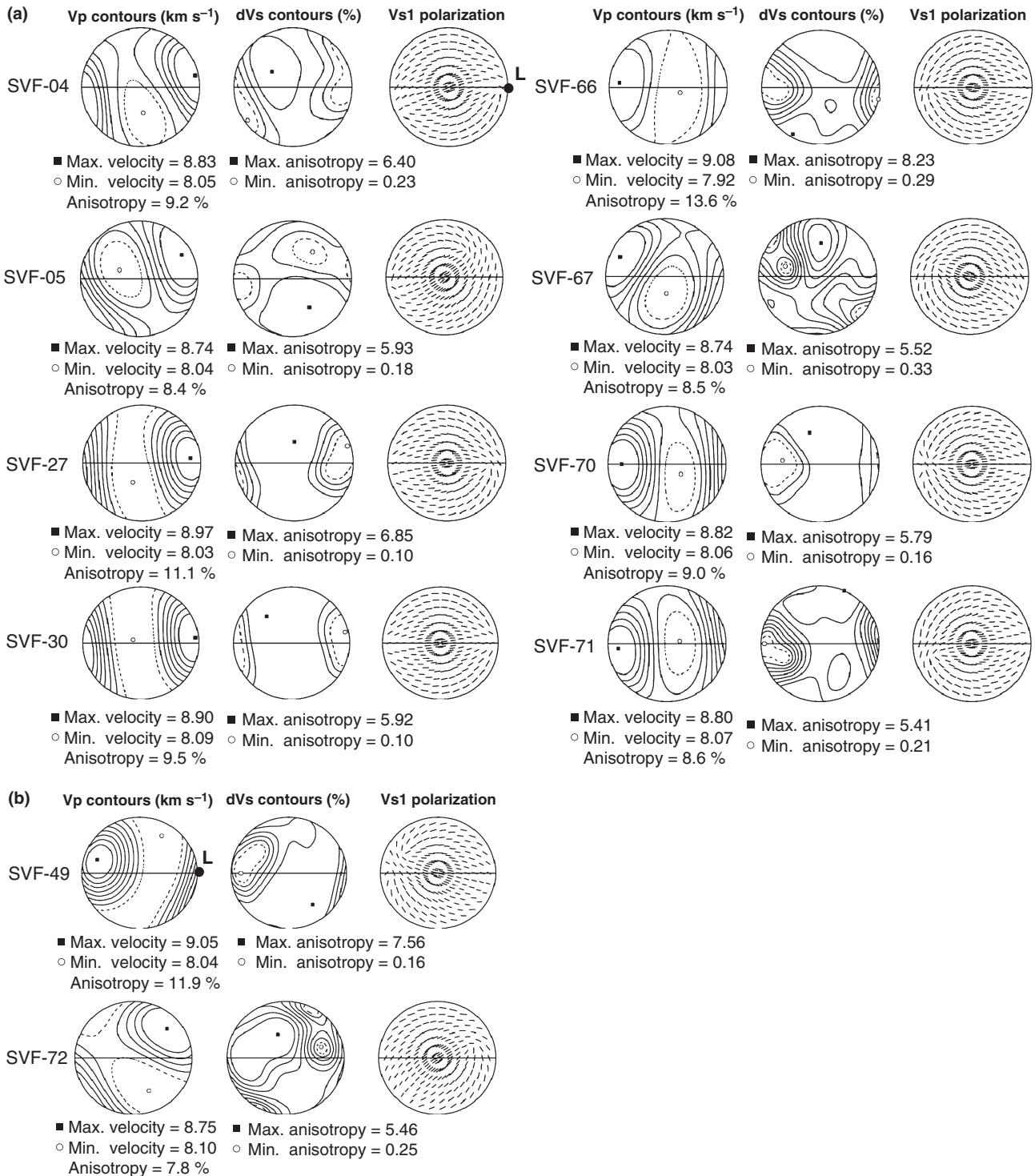


Fig. 9. Seismic anisotropy corresponding to the fabrics in the specimens showing a type A LPO (a) and type D LPO (b). The east–west direction corresponds to the lineation (L), and the centre of the plot corresponds to foliation normal. Azimuthal anisotropy of *P*-waves (Vp) and polarization anisotropy of *S*-waves are shown (dVs is a contour plot of the magnitude of shear wave polarization anisotropy and Vs1 is plot of the polarization direction of fast *S*-waves along different orientations of propagation). The centre of the figure corresponds to vertical propagation.

of water, and that the samples were dry, independent of the fabric type (types A and D LPOs). This observation was also in good agreement with previous

experimental studies (Bystricky *et al.*, 2000; Zhang *et al.*, 2000; Jung *et al.*, 2006), which showed that both types A and D LPOs of olivine were observed in

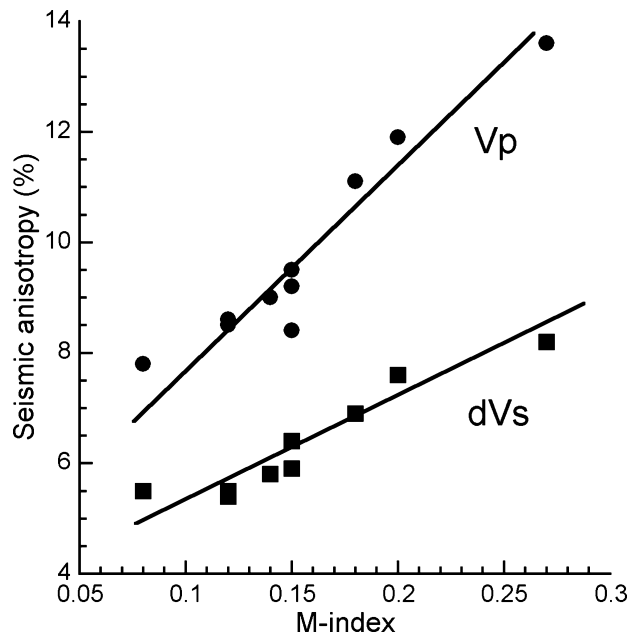


Fig. 10. The V_p anisotropy (%) and the max. dV_s anisotropy (%) as a function of LPO intensity (fabric strength defined by the M-index) for the olivine. dV_s is the magnitude of shear wave polarization anisotropy. Trend lines indicate tendencies and are not fitted functions.

a dry condition. All of the data, such as the LPOs, water contents, dislocation microstructures and grain sizes showed that there was good agreement between the microstructures of the natural rocks and experimental samples.

LPO strength

The strength of LPO of olivine was quantified using the M-index (Skemer *et al.*, 2005) and summarized in Table 1. The M-index quantifies the deviation of the uncorrelated misorientation angle distribution from a random misorientation distribution. The M-index varies between 0 for a random fabric and 1 for a single crystal. The M-index in our specimen was plotted as a function of seismic anisotropy (Fig. 10) and given in Table 1.

V_p seismic anisotropy increases with increasing M-index where a sharp increase of V_p anisotropy was observed at the M-index of 0.18. Polarization anisotropy of S-wave (dV_s) also increases with increasing M-index, but the slope is gentle compared to the V_p anisotropy (Fig. 10).

LPO of olivine and seismic anisotropy

The strong LPOs of the olivine (Fig. 4) and observation of the abundant dislocations and subgrain boundaries in the olivine (Fig. 6) indicate that the peridotites in Spitsbergen were deformed in dislocation creep. A calculation of the seismic anisotropy from the EBSD data for the olivine showed that the polarization

direction of the faster shear wave (V_{s1} polarization) was subparallel to the lineation (flow direction) in most samples. The fast polarization direction for vertical propagation in some samples (SVF-05, SVF-67 & SVF-72) diverges up to $\sim 40^\circ$ from the flow direction (Fig. 9). Pilidou *et al.* (2004, 2005) showed that the fast direction of the seismic anisotropy changes dramatically with depth. Beneath the study area, the nearly flow-parallel seismic anisotropy (V_{s1} polarization direction) of the present-day mantle flow (Pilidou *et al.*, 2005) at depths of ~ 75 – 100 km could be explained by the olivine type A or D LPO of (old) samples if the rocks were deformed in conditions similar to the present-day conditions. Our samples were equilibrated at ~ 10 kbar and 850 – 1000 °C. Furthermore, the samples showed a strong S-wave polarization anisotropy. As a result, we think that the seismic anisotropy at a depth of 75 km or less may be explained by the olivine fabrics (type A or D LPO) observed in this study. Seismic anisotropy at depths between 100 and 150 km becomes weak and the polarization direction of the faster S-wave deviates from the flow-parallel direction. The nearly flow-normal seismic anisotropy at a depth of ~ 150 km may be explained by the olivine type B LPO induced by high pressure in dry conditions (Jung *et al.*, 2009).

ACKNOWLEDGEMENTS

This study was supported by Grant R01-2007-000-20443-0, WCU R32-2008-000-10186-0 (H. J.) and KOPRI grant PE09100 (S. H. C.). This research was also partially supported by the BK21 at SEES, SNU. We thank M. Park, J. Lee and S. Jung for providing assistance at various stages of the project. We are most grateful to Prof. L. Dobrzhinetskaya and two anonymous reviewers for critical and constructive reviews of the manuscript.

REFERENCES

- Abramson, E.H., Brown, J.M., Slutsky, L.J. & Zaugg, J., 1997. The elastic constants of San Carlos olivine to 17 GPa. *Journal of Geophysical Research*, **102**, 12253–12263.
- Amundsen, H.E.F., Griffin, W.L. & O'Reilly, S., 1987. The lower crust and upper mantle beneath northwestern Spitsbergen: evidence from xenoliths and geophysics. *Tectonophysics*, **139**, 169–185.
- Banks, D., Sletten, R.S., Haldorsen, S., Dale, B., Heim, M. & Swensen, B., 1998. The thermal springs of Bockfjord, Svalbard: occurrence and major ion hydrochemistry. *Geothermics*, **27**, 445–467.
- Bell, D.R., Rossman, G.R., Maldener, J., Endisch, D. & Rauch, F., 2003. Hydroxide in olivine: a quantitative determination of the absolute amount and calibration of the IR spectrum. *Journal of Geophysical Research – Solid Earth*, **108**, ECV 8-1 ~ 8-9. doi: 10.1029/2001JB000679.
- Ben Ismail, W. & Mainprice, D., 1998. An olivine fabric database: an overview of upper mantle fabrics and seismic anisotropy. *Tectonophysics*, **296**, 145–157.
- Bertrand, P. & Mercier, J.-C., 1985. The mutual solubility of coexisting ortho- and clinopyroxene: toward an absolute

- geothermometer for the natural system. *Earth and Planetary Science Letters*, **76**, 109–122.
- Blackman, D.K., Wenk, H.R. & Kendall, J.M., 2002. Seismic anisotropy of the upper mantle I. Factors that affect mineral texture and effective elastic properties. *Geochemistry Geophysics Geosystems*, **3**, 1–24. doi: 10.1029/2001GC000248.
- Brey, G.P. & Köhler, T., 1990. Geothermobarometry in four-phase lherzolites II. New thermobarometers, and practical assessment of existing thermobarometers. *Journal of Petrology*, **31**, 1353–1378.
- Burov, Y.P. & Zagruzina, I.A., 1976. Results of the determination of the absolute age of Cenozoic basic rocks of the northern part of the Island of Spitsbergen. In: *Geol. Svalbarda* (ed Sokolov, V.N.), pp. 139–140, in Russian, Leningrad.
- Bystricky, M., Kunze, K., Burlini, L. & Burg, J.P., 2000. High shear strain of olivine aggregates: rheological and seismic consequences. *Science*, **290**, 1564–1567.
- Crane, K., Eldholm, O., Myhre, A.M. & Sundvor, E., 1982. Thermal implications for the evolution of the Spitsbergen transform fault. *Tectonophysics*, **89**, 1–32.
- Dingley, D.J., 1984. Diffraction from sub-micron areas using electron backscattering in a scanning electron microscope. *Scanning Electron Microscopy*, **2**, 569–575.
- Falus, G., Tommasi, A., Ingrin, J. & Szabo, C., 2008. Deformation and seismic anisotropy of the lithospheric mantle in the southeastern Carpathians inferred from the study of mantle xenoliths. *Earth and Planetary Science Letters*, **272**, 50–64.
- Fischer, K.M. & Wiens, D.A., 1996. The depth distribution of mantle anisotropy beneath the Tonga subduction zone. *Earth and Planetary Science Letters*, **142**, 253–260.
- Fouch, M.J. & Rondenay, S., 2006. Seismic anisotropy beneath stable continental interiors. *Physics of the Earth and Planetary Interiors*, **158**, 292–320.
- Frese, K., Trommsdorff, V. & Kunze, K., 2003. Olivine [100] normal to foliation: lattice preferred orientation in prograde garnet peridotite formed at high H₂O activity, Cima di Gagnone (Central Alps). *Contributions to Mineralogy and Petrology*, **145**, 75–86.
- Gifkins, R.C., 1970. *Optical Microscopy of Metals*. Elsevier, New York.
- Green, H.W. & Jung, H., 2005. Fluids, faulting, and flow. *Elements*, **1**, 31–37.
- Hess, H.H., 1964. Seismic anisotropy of the uppermost mantle under oceans. *Nature*, **203**, 629–631.
- Ionov, D.A., Bodinier, J.L., Mukasa, S.B. & Zanetti, A., 2002. Mechanisms and sources of mantle metasomatism: major and trace element compositions of peridotite xenoliths from Spitsbergen in the context of numerical modelling. *Journal of Petrology*, **43**, 2219–2259.
- Jung, H., 2009. Deformation fabrics of olivine in Val Malenco peridotite found in Italy and implications for the seismic anisotropy in the upper mantle. *Lithos*, **109**, 341–349.
- Jung, H. & Karato, S., 2001a. Water-induced fabric transitions in olivine. *Science*, **293**, 1460–1463.
- Jung, H. & Karato, S.I., 2001b. Effects of water on dynamically recrystallized grain-size of olivine. *Journal of Structural Geology*, **23**, 1337–1344.
- Jung, H., Katayama, I., Jiang, Z., Hiraga, T. & Karato, S., 2006. Effect of water and stress on the lattice-preferred orientation of olivine. *Tectonophysics*, **421**, 1–22.
- Jung, H., Mo, W. & Green, H.W., 2009. Upper mantle seismic anisotropy resulting from pressure-induced slip transition in olivine. *Nature Geoscience*, **2**, 73–77.
- Kaminski, E. & Ribe, N.M., 2001. A kinematic model for recrystallization and texture development in olivine polycrystals. *Earth and Planetary Science Letters*, **189**, 253–267.
- Karato, S., 1987. Scanning electron microscope observation of dislocations in olivine. *Physics and Chemistry of Minerals*, **14**, 245–248.
- Karato, S. & Jung, H., 2003. Effects of pressure on high-temperature dislocation creep in olivine. *Philosophical Magazine*, **A**, **83**, 401–414.
- Karato, S.I., Toriumi, M. & Fujii, T., 1980. Dynamic recrystallization of olivine single crystals during high-temperature creep. *Geophysical Research Letters*, **7**, 649–652.
- Karato, S., Jung, H., Katayama, I. & Skemer, P., 2008. Geodynamic significance of seismic anisotropy of the upper mantle: new insights from laboratory studies. *Annual Reviews*, **36**, 59–95.
- Katayama, I. & Karato, S., 2006. Effect of temperature on the B- to C-type olivine fabric transition and implication for flow pattern in subduction zones. *Physics of the Earth and Planetary Interiors*, **157**, 33–45.
- Katayama, I., Jung, H. & Karato, S., 2004. New type of olivine fabric from deformation experiments at modest water content and low stress. *Geology*, **32**, 1045–1048.
- Katayama, I., Karato, S.I. & Brandon, M., 2005. Evidence of high water content in the deep upper mantle inferred from deformation microstructures. *Geology*, **33**, 613–616.
- Kohlstedt, D.L., Goetze, C., Durham, W.B. & Vander Sande, J., 1976. New technique for decorating dislocations in olivine. *Science*, **191**, 1045–1046.
- Kohlstedt, D.L., Keppler, H. & Rubie, D.C., 1996. Solubility of water in the alpha, beta and gamma phases of (Mg, Fe)₂SiO₄. *Contributions to Mineralogy and Petrology*, **123**, 345–357.
- Lloyd, G.E., 1987. Atomic number and crystallographic contrast images with the SEM: a review of backscattered electron techniques. *Mineralogical Magazine*, **51**, 3–19.
- Long, M.D. & Silver, P.G., 2008. The subduction zone flow field from seismic anisotropy: a global view. *Science*, **319**, 315–318.
- Long, M.D. & van der Hilst, R.D., 2005. Upper mantle anisotropy beneath Japan from shear wave splitting. *Physics of the Earth and Planetary Interiors*, **151**, 206–222.
- Mainprice, D., 1990. A fortran program to calculate seismic anisotropy from the lattice preferred orientation of minerals. *Computers and Geosciences*, **16**, 385–393.
- Mainprice, D. & Silver, P.G., 1993. Interpretation of SKS-waves using samples from the subcontinental lithosphere. *Physics of the Earth and Planetary Interiors*, **78**, 257–280.
- Mainprice, D., Barruol, G. & Ismail, W.B., 2000. The seismic anisotropy of the earth's mantle from single crystal to polycrystal. In: *Earth's Deep Interior* (eds Karato, S., Forte, A.M., Liebermann, R.C., Masters, G. & Stixrude, L.), pp. 237–264, Geophysical Monograph, 117, American Geophysical Union, Washington, DC.
- Mehl, L., Hacker, B.R., Hirth, G. & Kelemen, P.B., 2003. Arc-parallel flow within the mantle wedge: evidence from the accreted Talkeetna arc, south central Alaska. *Journal of Geophysical Research – Solid Earth*, **108**, ESE 4-1 ~ 4-18. doi: 10.1029/2002JB002233.
- Mercier, J.C., 1985. Olivine and pyroxene. In: *Preferred Orientation in Deformed Metals and Rocks: An Introduction to Modern Texture Analysis* (ed. Wenk, H.R.), pp. 407–430, Academic Press, INC, New York.
- Mercier, J.-C.C. & Nicolas, A., 1975. Textures and fabrics of upper-mantle peridotites as illustrated by xenoliths from basalts. *Journal of Petrology*, **16**, 454–487.
- Michibayashi, K., Tasaka, M., Ohara, Y., Ishii, T., Okamoto, A. & Fryer, P., 2007. Variable microstructure of peridotite samples from the southern Mariana Trench: evidence of a complex tectonic evolution. *Tectonophysics*, **444**, 111–118.
- Mizukami, T., Wallis, S.R. & Yamamoto, J., 2004. Natural examples of olivine lattice preferred orientation patterns with a flow normal a-axis maximum. *Nature*, **427**, 432–436.
- Möckel, J.R., 1969. Structural petrology of the garnet-peridotite of Alpe Arami (Ticino, Switzerland). *Leidse Geologische Mededelingen*, **42**, 61–130.
- Nakajima, J. & Hasegawa, A., 2004. Shear-wave polarization anisotropy and subduction-induced flow in the mantle wedge

- of northeastern Japan. *Earth and Planetary Science Letters*, **225**, 365–377.
- Nicolas, A. & Christensen, N.I., 1987. Formation of anisotropy in upper mantle peridotites: a review. *American Geophysical Union*, **16**, 111–123.
- Nicolas, A. & Poirier, J.P., 1976. *Crystalline Plasticity and Solid State Flow in Metamorphic Rocks*. John Wiley & Sons, New York, 444 pp.
- Nicolas, A., Bouchez, J.L., Boudier, F.M. & Mercier, J.C., 1971. Textures, structures and fabrics due to solid state flow in some European lherzolites. *Tectonophysics*, **12**, 55–85.
- Panozzo, R., 1984. Two-dimensional strain from the orientation of lines in a plan. *Journal of Structural Geology*, **6**, 215–221.
- Park, J. & Levin, V., 2002. Geophysics – Seismic anisotropy: tracing plate dynamics in the mantle. *Science*, **296**, 485–489.
- Paterson, M.S., 1982. The determination of hydroxyl by infrared absorption in quartz, silicate glasses and similar materials. *Bulletin Mineralogist*, **105**, 20–29.
- Pilidou, S., Priestley, K., Gudmundsson, O. & Debayle, E., 2004. Upper mantle S-wave speed heterogeneity and anisotropy beneath the North Atlantic from regional surface wave tomography: the Iceland and Azores plumes. *Geophysical Journal International*, **159**, 1057–1076.
- Pilidou, S., Priestley, K., Debayle, E. & Gudmundsson, O., 2005. Rayleigh wave tomography in the North Atlantic: high resolution images of the Iceland, Azores and Eifel mantle plumes. *Lithos*, **79**, 453–474.
- Prior, D.J., Boyle, A.P., Brenker, F. *et al.*, 1999. The application of electron backscatter diffraction and orientation contrast imaging in the SEM to textural problems in rocks. *American Mineralogist*, **84**, 1741–1759.
- Savage, M.K., 1999. Seismic anisotropy and mantle deformation: what have we learned from shear wave splitting? *Reviews of Geophysics*, **37**, 65–106.
- Silver, P.G., 1996. Seismic anisotropy beneath the continents: probing the depths of geology. *Annual Review of Earth and Planetary Sciences*, **24**, 385–432.
- Skemer, P. & Karato, S.I., 2008. Sheared lherzolite xenoliths revisited. *Journal of Geophysical Research – Solid Earth*, **113**, 1–14. doi: 10.1029/2007JB005286.
- Skemer, P., Katayama, I., Jiang, Z. & Karato, S.-I., 2005. The misorientation index: development of a new method for calculating the strength of lattice-preferred orientation. *Tectonophysics*, **411**, 157–167.
- Skemer, P., Katayama, I. & Karato, S.I., 2006. Deformation fabrics of the Cima di Gagnone peridotite massif, Central Alps, Switzerland: evidence of deformation at low temperatures in the presence of water. *Contributions to Mineralogy and Petrology*, **152**, 43–51.
- Skjeltkvale, B.L., Amundsen, H.E.F., O’Reilly, S.Y., Griffin, W.L. & Gjelsvik, T., 1989. A primitive alkali basaltic stratovolcano and associated eruptive centers, Northwestern Spitsbergen: volcanology and tectonic significance. *Journal of Volcanology and Geothermal Research*, **37**, 1–19.
- Smith, G.P., Wiens, D.A., Fischer, K.M., Dorman, L.M., Webb, S.C. & Hildebrand, J.A., 2001. A complex pattern of mantle flow in the Lau backarc. *Science*, **292**, 713–716.
- Sundberg, M. & Cooper, R.F., 2008. Crystallographic preferred orientation produced by diffusional creep of harzburgite: effects of chemical interactions among phases during plastic flow. *Journal of Geophysical Research – Solid Earth*, **113**, 1–16. doi: 10.1029/2008jb005618.
- Tommasi, A., Mainprice, D., Canova, G. & Chastel, Y., 2000. Viscoplastic self-consistent and equilibrium-based modeling of olivine lattice preferred orientations: implications for the upper mantle seismic anisotropy. *Journal of Geophysical Research – Solid Earth*, **105**, 7893–7908.
- Tuchschmid, M. & Spillmann, P., 1992. Neogene and Quaternary volcanism on Spitsbergen – the revival of an Arctic hot spot. *Schweizerische Mineralogische und Petrographische Mitteilungen*, **72**, 251–270.
- Vågnes, E. & Amundsen, H.E.F., 1993. Late Cenozoic uplift and volcanism on Spitsbergen; caused by mantle convection? *Geology*, **21**, 251–254.
- van der Wal, D., Chopra, M., Druary, M. & Fitz Gerald, J., 1993. Relationships between dynamically recrystallized grain size and deformation conditions in experimentally deformed olivine rocks. *Geophysical Research Letters*, **20**, 1479–1482.
- Warren, J.M., Hirth, G. & Kelemen, P.B., 2008. Evolution of olivine lattice preferred orientation during simple shear in the mantle. *Earth and Planetary Science Letters*, **272**, 501–512.
- Wells, P.R.A., 1977. Pyroxene thermometry in simple and complex systems. *Contributions to Mineralogy and Petrology*, **62**, 129–139.
- Wenk, H.R., 2002. Texture and anisotropy. In: *Plastic Deformation of Minerals and Rocks. Reviews in Mineralogy and Geochemistry*, Vol. **51** (eds Karato, S.-I. & Wenk, H.-R.), pp. 291–329. Mineralogical Society of America, Washington, DC.
- Xu, Z., Wang, Q., Ji, S. *et al.*, 2006. Petrofabrics and seismic properties of garnet peridotite from the UHP Sulu terrane (China): implications for olivine deformation mechanism in a cold and dry subducting continental slab. *Tectonophysics*, **421**, 111–127.
- Zhang, S. & Karato, S., 1995. Lattice preferred orientation of olivine aggregates deformed in simple shear. *Nature*, **375**, 774–777.
- Zhang, S.Q., Karato, S., Fitz Gerald, J.D., Faul, U.H. & Zhou, Y., 2000. Simple shear deformation of olivine aggregates. *Tectonophysics*, **316**, 133–152.

SUPPORTING INFORMATION

Additional Supporting Information may be found in the online version of this article:

Table S1. Mineral compositions and temperature estimates for Spitsbergen peridotites.

Please note: Wiley-Blackwell are not responsible for the content or functionality of any supporting materials supplied by the authors. Any queries (other than missing material) should be directed to the corresponding author for the article.

Received 7 March 2009; revision accepted 23 June 2009.